

STRUCTURE OF THE MID-INFRARED-EMITTING DISK AROUND WL 16

MICHAEL E. RESSLER¹

Jet Propulsion Laboratory, California Institute of Technology, MS 169-327, 4800 Oak Grove Drive, Pasadena, CA 91109

AND

MARY BARSONY^{1,2,3}

Space Science Institute, 3100 Marine Street, Suite A353, Boulder, CO 80303-1058

Received 2002 May 16; accepted 2002 October 31

ABSTRACT

WL 16 is a unique member of the embedded young stellar population in the nearby ρ Ophiuchi cloud core: its extended, high surface brightness disk is visible only at mid-infrared wavelengths. We present diffraction-limited images, from 7.9 to 24.5 μm , of WL 16 acquired at the Keck II telescope. We take advantage of the $\sim 0\prime\prime.3$ angular resolution of the mid-infrared images to derive physical parameters for the central object by self-consistently combining them with available near-infrared spectroscopy, point-spread function fit photometry, and pre-main-sequence evolutionary tracks. We find the central star to be a 250 L_{\odot} , 4 M_{\odot} , Herbig Ae star, seen through foreground material of the ρ Oph cloud core that provides an extinction of $A_V = 31 \pm 1$ mag. WL 16's disk is detected through all nine observed passbands, not only those four that sample polycyclic aromatic hydrocarbon (PAH) emission features. We confirm, therefore, that the emitting particles are composed of both PAHs and very small (5–100 Å) graphitic grains. The disk size as observed through the four PAH filters is $7\prime\prime \times 3\prime\prime.5$, corresponding to a disk diameter of ~ 900 AU. The disk's major axis is at a position angle of $60^{\circ} \pm 2^{\circ}$ and is viewed at an inclination angle of $62.2^{\circ} \pm 0.4^{\circ}$ to our line of sight. Our derived inclination angle is in excellent agreement with the inclination previously inferred for the inner disk ($R \leq 30 R_{\odot}$) from kinematic modeling of the near-infrared spectral lines of CO. We can distinguish structure within the PAH disk at unprecedented resolution. We confirm a resolved ($1\prime\prime.5$ diameter) core component at 7.9 and 8.8 μm due to emission from positively charged PAHs. An enhancement in the emission at 12.5 μm at the disk's edges is found for the first time and signals the presence of larger (≥ 50 –80 carbon atoms) and/or more hydrogenated PAHs than those found in the bulk of the disk. We find a disk asymmetry, observed at all nine mid-infrared wavelengths, at projected radii $1\prime\prime$ – $2\prime\prime.5$ (corresponding to $125 \text{ AU} \leq r \leq 300 \text{ AU}$) from the central source.

Subject headings: circumstellar matter — dust, extinction — infrared: ISM — stars: formation — stars: individual (WL 16) — stars: pre-main-sequence

1. INTRODUCTION

WL 16 was first discovered, via near-infrared photometry (Wilking & Lada 1983), to be a member of the deeply embedded cluster currently forming in the highest extinction core of the nearby ρ Ophiuchi cloud (Barsony et al. 1997 and references therein); it is undetectable at optical wavelengths. WL 16 was identified as a few times 10^5 yr old, late-stage protostar, based on its rising infrared (2–60 μm) spectral slope, and was assumed to consist of a remnant infalling dust and gas envelope surrounding a central protostar+disk system (Lada 1987; Adams, Lada, & Shu 1987; Wilking, Lada, & Young 1989).

Subsequent observations conflicted with the classification of WL 16 as a late-stage protostar, however. WL 16 lacks, by 2 orders of magnitude, the amount of millimeter flux expected from a low-mass young stellar object (YSO) at such an early evolutionary stage, and it shows no evidence

of a molecular outflow (Cabrit & André 1991; André & Montmerle 1994). WL 16 is the only source in Ophiuchus known to exhibit the entire suite of polycyclic aromatic hydrocarbon (PAH) emission features (Tanaka et al. 1990; Hanner, Tokunaga, & Geballe 1992; Deutsch et al. 1995; Natta & Krügel 1995). It has become clear that PAH emission accounts for the appearance of WL 16's mid-infrared spectral features, rather than what had previously been interpreted as a deep silicate absorption feature (Hanner et al. 1992), such as is generally associated with the presence of a cool circumstellar envelope in late-stage, low-mass ($\leq 2 M_{\odot}$) protostars.

WL 16 is also the first YSO in which the presence of a hot ($1000 \text{ K} \leq T \leq 6000 \text{ K}$), dense, neutral, gaseous, Keplerian disk was inferred via detailed modeling of its 2.3 μm CO overtone emission-line shapes (Dent & Geballe 1991; Carr et al. 1993; Chandler et al. 1993; Chandler, Carlstrom, & Scoville 1995). The inner disk (3–30 R_{\odot}) around WL 16 is modeled as having a high inclination angle ($>48^{\circ}$) with a fairly low accretion rate from the disk to the star of $\dot{M} \sim 2 \times 10^{-7} M_{\odot} \text{ yr}^{-1}$ (Najita et al. 1996a). Velocity-resolved spectroscopy of the Br γ hydrogen line toward WL 16 provides independent evidence of the low accretion rate infalling gas at spatial scales smaller than that of the inner disk radius (Najita, Carr, & Tokunaga 1996b; Hartmann, Hewett, & Calvet 1994).

¹ Visiting Astronomer at the W. M. Keck Observatory, which is operated as a scientific partnership among the California Institute of Technology, the University of California, and the National Aeronautics and Space Administration. The Observatory was made possible by the generous financial support of the W. M. Keck Foundation.

² NSF POWRE Visiting Professor, Physics Department, Harvey Mudd College, Claremont, CA 91711.

³ NSF Career Award Recipient.

What makes WL 16 truly unique, however, is the large extent ($8''$ along its major axis) of its elliptically shaped mid-infrared emission, as revealed by previous imaging studies (Deutsch et al. 1995; Emerson et al. 1996; Moore et al. 1998). Spatially resolved mid-infrared spectroscopy of this elongated dust structure has confirmed the presence of both very small grains (VSGs) and PAHs throughout (DeVito & Hayward 1998).

The presence of mid-infrared emission out to such large extents from a central source is not expected from “classical” or “standard equilibrium emitting” silicate and amorphous carbon, or “MRN,” grains (Mathis, Rumpl, & Nordsieck 1977). These “standard” grains range in size from 10 to ≥ 250 nm, have a size distribution $n(a) \propto a^{-3.5}$, and are generally assumed to be large enough to come into equilibrium with the surrounding radiation field (but see Lynch & Mazuk 2000 for a thorough discussion of the shortcomings attendant on this assumption).

By contrast, the so-called graphitic VSGs, which range in size from $0.4 \text{ nm} \leq a \leq 10 \text{ nm}$ with a size distribution $n(a) \propto a^{-4}$ (Draine & Anderson 1985), and the PAHs, which contain 25–40 carbon atoms, or PAH clusters, containing 50–500 carbon atoms (Siebenmorgen & Krügel 1992), are heated and emit in a nonequilibrium fashion. They are therefore capable of emitting in the mid-infrared, at large distances from a central illuminating source at (seemingly) high temperatures not in equilibrium with the surrounding radiation field.

Detailed radiative transfer modeling of the spectral energy distribution of physically realistic, spherically symmetric dust shells surrounding Herbig Ae stars shows that whereas the mid-infrared ($\sim 2\text{--}20 \mu\text{m}$) emission from classical grains is negligible, the continuum emission from VSGs in this wavelength range accounts for all of the observed mid-infrared excesses (above photospheric) for these sources (Natta, Prusti, & Krügel 1993). These authors also note that VSGs do not emit in the *J* band ($1.25 \mu\text{m}$) and emit only very little in the *H* band ($1.65 \mu\text{m}$) for the same models in which VSGs contribute essentially all of the observed mid-infrared continuum emission. Therefore, the slope of the spectrum in the $1.25\text{--}1.65 \mu\text{m}$ continuum is effectively determined by the underlying stellar radiation field and by the absorption and scattering properties of the standard grains, even in the presence of VSGs.

Whereas VSGs essentially determine the mid-infrared continuum emission in the circumstellar environments of Herbig Ae/Be stars (Herbig 1994), the effect of adding PAH emitters results in emission into several well-defined, solid-state features, with minimal change in the underlying shape of the mid-infrared continuum, as compared with models computed in the absence of PAHs. When a UV/visible photon from the central source interacts with a PAH lattice, the photon energy is redistributed into stretching and bending modes of C—H and C=C bonds; these modes reemit energy in broad, solid-state features. These well-known PAH features are centered at $3.29 \mu\text{m}$ (the $v = 1 \rightarrow 0$ C—H stretch), 6.2 and $7.7 \mu\text{m}$ (C=C stretch modes), $8.6 \mu\text{m}$ (C—H in-plane bend), $11.3 \mu\text{m}$ (C—H out-of-plane bend), and $12.5 \mu\text{m}$ (C—H bond resonance) (Tokunaga et al. 1991; Siebenmorgen & Krügel 1992; Brooke, Tokunaga, & Strom 1993; Hanner, Brooke, & Tokunaga 1995). The region between 10 and $20 \mu\text{m}$ is dominated by a resonance in the range $10.5 \mu\text{m} \leq \lambda \leq 13.5 \mu\text{m}$ (encompassing the 11.3 and $12.5 \mu\text{m}$ features) due to C—H out-of-plane bending.

Although the approximate wavelength of one resonance due to a mono C—H vibration is about $11.3 \mu\text{m}$, this wavelength can actually be longer, depending on hydrogenation (the number of H atoms attached to the edge carbon rings). Some continuum emission is also produced by the overlapping wings of these PAH features.

The excitation of mid-infrared emission by PAHs and VSGs out to such large physical distances from the central object as observed in WL 16 requires both a fairly luminous source of optical/UV photons and optically thin paths from the central object to the mid-IR-emitting regions. The uniqueness of the mid-IR-emitting structure observed in WL 16 among all of the known embedded sources in ρ Oph, combined with the fact that many intermediate-mass ($2 M_{\odot} \leq M \leq 8 M_{\odot}$) YSOs show PAH feature emission (Waters & Waelkens 1998), leads one to reconsider the central source’s properties.

In order to shed further light on both the nature of the central object and its surrounding circumstellar material, we have obtained images of WL 16 at nine distinct wavelengths—through filters that variously either include or exclude PAH feature emission and span the $8\text{--}25 \mu\text{m}$ atmospheric windows—all at unprecedentedly high spatial resolution ($\sim 0''.3$). In addition, we have made use of previously published near-infrared photometry, recently published spectroscopy, and up-to-date pre-main-sequence (PMS) tracks for intermediate stellar masses to reexamine the nature of the central object.

2. OBSERVATIONS

We observed WL 16 with JPL’s mid-infrared camera, MIRLIN (Ressler et al. 1994), at the visitor port of the Keck II Telescope on UT 1998 March 14 and 1999 January 27. The sky was clear and dry on both nights ($\tau_{225\text{GHz}} \sim 0.06$ and 0.04 , respectively). MIRLIN employs a Boeing HF-16, 128×128 pixel, Si:As impurity band conductor detector array and produces a plate scale of $0''.138 \text{ pixel}^{-1}$ ($17''.5$ field of view) with the *f*/40 chopping secondary mirror at Keck II.

Background subtraction was performed by chopping the telescope secondary mirror $8''$ in a north-south direction, then nodding the entire telescope $30''$ east-west, completely off the source, in order to remove residual differences. Observations were performed through the six $10 \mu\text{m}$ “silicate” filters (7.9 , 8.8 , 9.7 , 10.3 , 11.7 , and $12.5 \mu\text{m}$) and the $17.9 \mu\text{m}$ filter on 1998 March 14, and through the 20.8 and $24.5 \mu\text{m}$ filters on 1999 January 27. All of these filters have a passband of $\Delta\lambda/\lambda \approx 10\%$, except for $24.5 \mu\text{m}$, where $\Delta\lambda/\lambda \approx 3\%$. Plots of the nine filter passbands are shown in Figure 1, along with the continuum-subtracted mid-infrared spectrum of WL 16 (DeVito & Hayward 1998), to indicate how the PAH emission features were sampled. Note that the well-known broad silicate features due to the Si—O stretching and bending modes at 9.7 and $18 \mu\text{m}$, respectively, were also sampled.

Total on-source integration times through each of the silicate filters were approximately 30 s — 200 co-added chop pairs of roughly 80 ms duration in each of the two beams. Total on-source integration times through the longer wavelength filters were 2.0 , 2.7 , and 2.4 minutes through the 17.9 , 20.8 , and $24.5 \mu\text{m}$ filters, respectively. The primary photometric standard and point-spread function (PSF) calibrator was the A3 V star, β Leo, which has a magnitude ranging

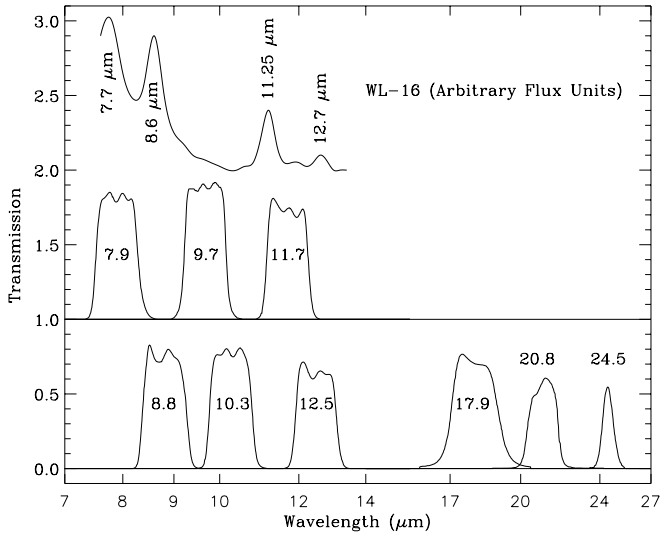


FIG. 1.—MIRLIN filter transmission curves, with a continuum-subtracted spectrum of WL 16 (DeVito & Hayward 1998). The filter curves are reproduced from the manufacturer's data taken at 77 K. The filters at 7.9, 9.7, and 11.7 μm have had their baselines shifted by 1 for clarity. The 9.7 and 10.3 μm filters sample the “continuum” reasonably cleanly, while the 7.9, 8.8, 11.7, and 12.5 μm filters each sample a PAH feature.

from 1.91 to 1.84 from 7 to 13 μm . The calibrator at 17.9 and 20.8 μm was α Hya, a K3 III star with a magnitude of -1.49 ; the standard at 24.5 μm was β Lib, a 2.84 mag B8 V star. Consistency checks were performed with α CMA (-1.39 mag) and σ Sco (~ 2.40 mag); the latter proved to be

an easily resolved binary with $0''.45$ separation. Atmospheric extinction was corrected by observing the calibrators at several different air masses. The resulting coefficients were found to be quite low (< 0.1 – 0.2 mag per air mass).

3. RESULTS

3.1. Mid-Infrared Images

The mid-infrared images of WL 16 are presented in Figure 2. It is clear that the circumstellar structure surrounding WL 16 appears brighter with respect to the central source in the filters that encompass the PAH features, relative to its appearance in the filters that exclude PAH feature emission over the 7–13 μm region. Nevertheless, the mid-infrared emission is still well resolved, even in the filters that exclude PAH feature emission.

The extent of the emission derived from the images that include the PAH features is $7'' \times 3''.5$ at 1% of the peak level. This projected source size corresponds to 880×440 AU for an assumed distance of $d = 125$ pc (de Geus, de Zeeuw, & Lub 1989; de Geus 1992; Knude & Høg 1998). The position angle of the major axis, measured east from north, is $60^\circ \pm 2^\circ$.

Intensity profiles along the major axis of WL 16 (indicated on the 12.5 μm image of Fig. 2) are presented for each wavelength in Figure 3. The central, bright core is resolved at the shortest (7.9 and 8.8 μm) wavelengths, but is unresolved at wavelengths longer than this. We also find that the contrast of the central peak to the disk emission varies with wavelength (see col. [5] of Table 1), with the highest

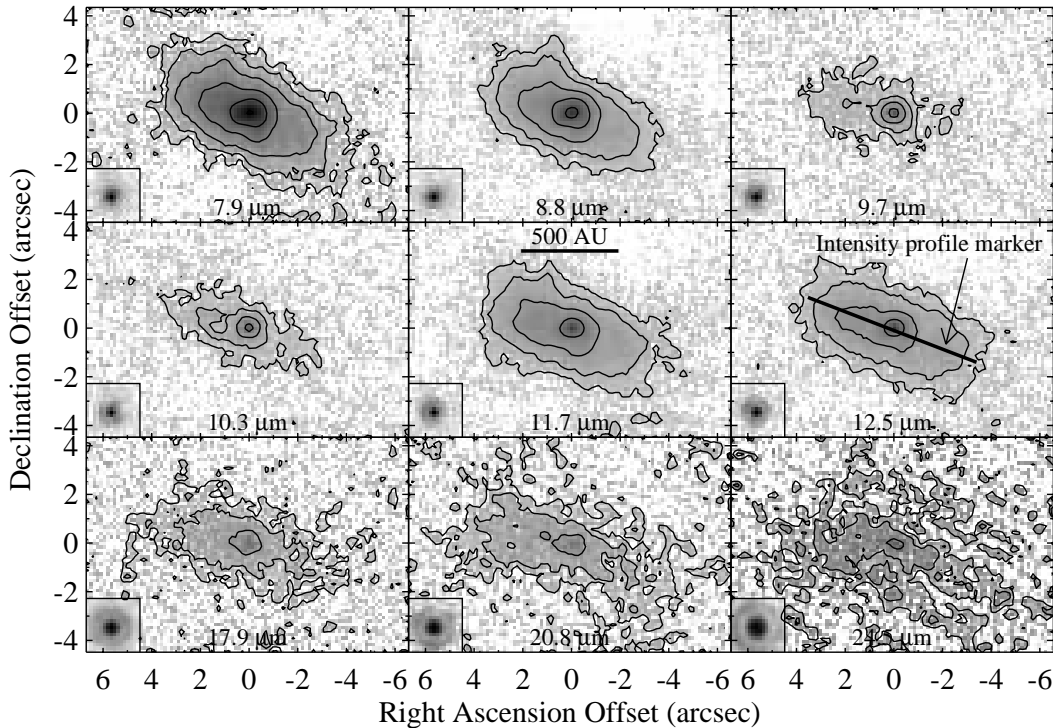


FIG. 2.—Images of WL 16 at all observed mid-infrared wavelengths. North is up, east is left for all images. The pixel scale is $0''.138$ pixel $^{-1}$, giving the frames a roughly $13'' \times 9''$ field of view. The PSF calibrators (*insets*) were β Leo at $\lambda < 13$ μm and α Hya at longer wavelengths. Contours in each panel represent the flux density in Jy arcsec $^{-2}$ and are spaced by 1 mag. The lowest contour level in all images starts at 50 mJy arcsec $^{-2}$; subsequent contour levels are at 0.125, 0.315, 0.792, 1.9, and 5.0 Jy arcsec $^{-2}$. The FWHMs of the PSFs at each wavelength are the diffraction-limited values of $0''.17$ at 7.9 μm , $0''.19$ at 8.8 μm , $0''.21$ at 9.7 μm , $0''.22$ at 10.3 μm , $0''.25$ at 11.7 μm , $0''.27$ at 12.5 μm , $0''.39$ at 17.9 μm , $0''.45$ at 20.8 μm , and $0''.53$ at 24.5 μm . The “intensity profile marker” in the 12.5 μm image shows the axis along which the brightness profiles of Fig. 3 are plotted.

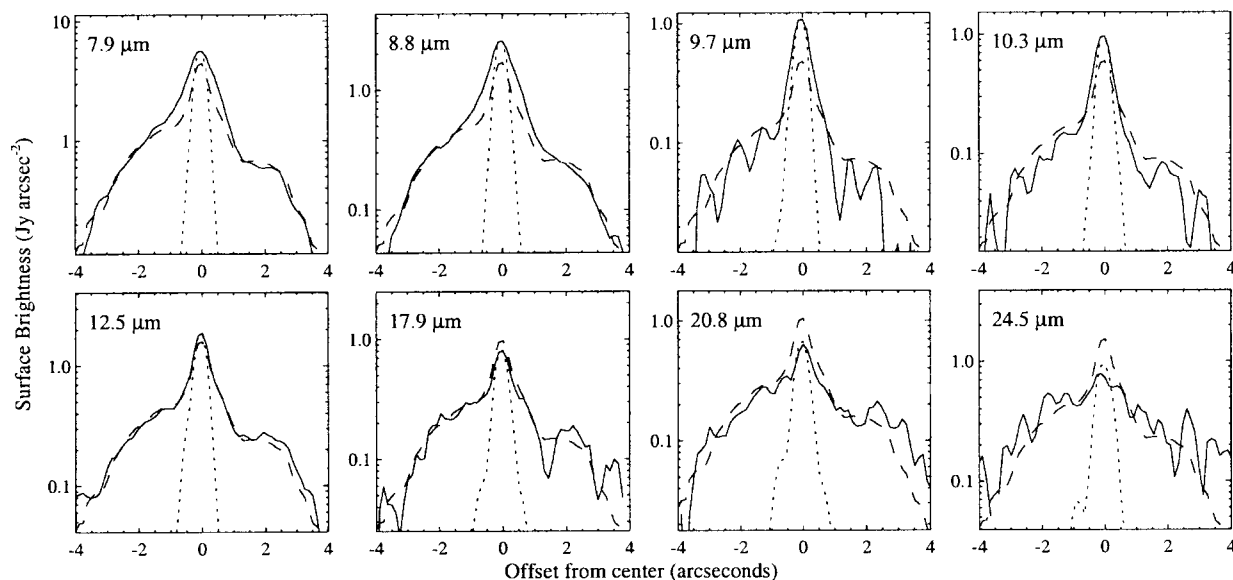


FIG. 3.—Intensity profiles along the disk’s major axis at all observed wavelengths. *Solid curves*, Intensity profiles; *dotted curves*: PSF profiles; *dashed curves*: scaled profiles at $11.7 \mu\text{m}$ (normalized at a point in the “shoulder” $1''.5$ northeast from the center).

PSF/disk contrast occurring in the 9.7 and $10.3 \mu\text{m}$ images and the lowest PSF/disk contrast in the $24.5 \mu\text{m}$ image.

3.2. Mid-Infrared Color Ratios

In Figure 4, we present three mid-infrared color ratio images of the WL 16 disk: the $7.9/8.8 \mu\text{m}$ flux ratios in the top left panel, the $8.8/11.7 \mu\text{m}$ flux ratios in the middle left panel, and the $12.5/11.7 \mu\text{m}$ flux ratios in the bottom left

panel. We find no significant color gradient in the entire $7.9/8.8 \mu\text{m}$ flux ratio image. This is in contrast to the other two flux ratio images presented in Figure 4. The $8.8/11.7 \mu\text{m}$ image (and the $7.9/11.7 \mu\text{m}$ image not shown here) shows significantly enhanced values within the inner $\sim 1''.5$ diameter “core” (see also the corresponding panels of Fig. 3). This inner-core flux ratio enhancement is more quantitatively illustrated in the corresponding crosscut panel of Figure 4, which shows the $8.8/11.7 \mu\text{m}$ flux ratio at a peak

TABLE 1
PHOTOMETRY OF WL 16

Wavelength (μm) (1)	PSF Fit Flux (Jy) (2)	Aperture Flux ^a (Jy) (3)	Previously Published Flux (Jy) (4)	Disk/PSF Ratio [(Aperture–PSF)/PSF] (5)	References (6)
1.2.....	0.0037	...	0.0040	...	1, 2
1.65.....	0.059	...	0.071	...	1, 2
2.2.....	0.45	...	0.48	...	1, 2
3.4.....	1.17	...	1.36	...	1, 2
3.8.....	1.22	1
4.8.....	2.18	...	2.02	...	1, 3
7.9.....	1.49	19.13	...	11.8	...
8.8.....	0.65	7.89	8.3	11.1	3
9.7.....	0.35	2.18	1.6	5.2	3
10.3.....	0.30	1.97	1.8	5.5	3
11.7.....	0.49	7.07	7.1	13.4	3
12.5.....	0.57	6.30	6.25	10.1	3
17.9.....	0.28	4.53	...	15.2	...
20.8.....	0.25	3.19	4.8 ^b	11.8	3
24.5.....	0.19	5.67	...	28.8	...
12.....	...	16.0 (HIRES)	18.8	...	4
25.....	...	14.4 (HIRES)	<40	...	4
60.....	...	129 (HIRES)	202	...	4
100.....	...	223 (HIRES)	4
1300.....	<0.006	...	5

^a All quoted fluxes are for an $8''$ diameter aperture, except for HIRES fluxes, which were determined from a $45''$ diameter aperture after local background subtraction.

^b Broadband Q measurement, $\Delta\lambda/\lambda \sim 40\%$.

REFERENCES.—(1) Ressler 1992; (2) Wilking & Lada 1983; (3) Lada & Wilking 1984; (4) Young, Lada, & Wilking 1986; (5) Motte, André, & Neri 1998.

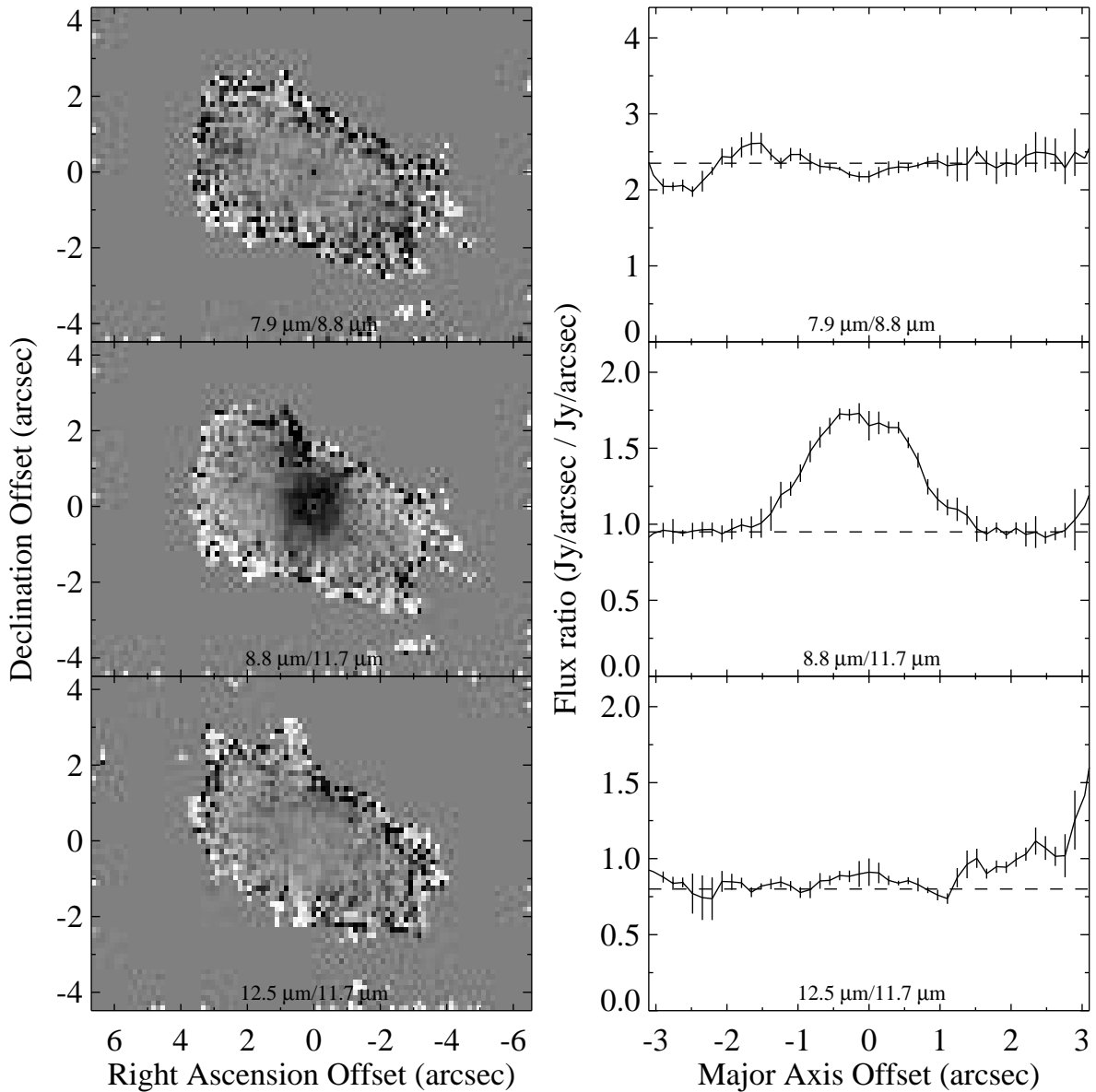


FIG. 4.—Color ratio images of WL 16 (*left*) and corresponding crosscuts (*right*) taken along the disk’s major axis for selected wavelength pairs: 7.9/8.8 μm (*top*), 8.8/11.7 μm (*middle*), and 12.5/11.7 μm (*bottom*). North is up, east is left. The pixel scale is $0''.138 \text{ pixel}^{-1}$, giving a $13'' \times 9''$ field of view. The images were divided on a pixel-by-pixel basis and are presented unsmoothed. In the right-hand panels, we plot the corresponding flux ratios along the major axis as a function of angular distance from the central source. The ratio images were rotated by 30° ; then the median and standard deviation were computed from a 7 pixel ($1''.0$) wide strip centered on the major axis and plotted accordingly.

value of ~ 1.75 within the inner core, declining to a relatively constant value of ~ 0.95 outside this core. By contrast, the 12.5/11.7 μm flux ratio image shows little variation in the inner ($\leq 2''$) regions, but shows a small enhancement toward the disk’s edges. This flux ratio rises from a value of ≈ 0.85 in the inner regions to values ≥ 1.1 at the disk’s outer edges.

3.3. Photometry

We present new mid-infrared and far-infrared photometry for WL 16 in Table 1. To compare our photometry with previous ground-based results (see, e.g., Lada & Wilking 1984; Moore et al. 1998), we have performed false aperture photometry with an $8''$ diameter software aperture. In general, the agreement between our $8''$ aperture photometry and that of Lada & Wilking (1984) is quite good in the

mid-infrared. The random errors in our flux measurements are about 3% at 8–13 μm , 7% at 17.9 and 20.8 μm , and 30% at 24.5 μm . Our fluxes agree with those previously published to 2σ at 8.8 μm , 3σ at 10.3 μm , and less than 1σ at 11.7 and 12.5 μm . We find some discrepancy, however, between our 9.7 μm flux (2.2 Jy) and the previously published 9.7 μm flux (1.6 Jy) of Lada & Wilking (1984), although this may not be significant because of the strong, telluric ozone absorption feature contained within this band.

We also performed PSF fit photometry of the central peak in each image of WL 16 to better determine the flux from just the central source, since the spatial resolution of the mid-infrared images allows a clean separation of the central peak from the surrounding nebulosity. To accomplish this, a PSF image derived from observed standard stars at each wavelength was shifted, scaled, and offset to fit

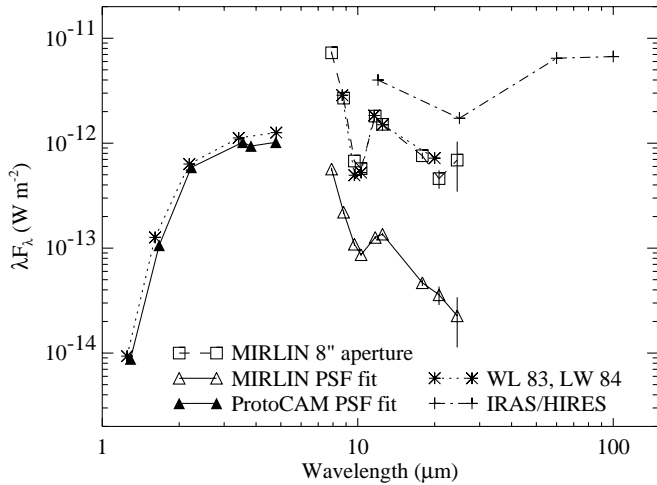


FIG. 5.—Observed SEDs of WL 16. Triangles connected by a solid curve represent measurements derived from PSF fitting (filled triangles are for near-infrared data from Ressler 1992; open triangles are for mid-infrared data from this work). Fluxes derived from our aperture photometry (using 8'' software apertures) are plotted as squares connected with a dashed curve. Data from Wilking & Lada (1983) and Lada & Wilking (1984) are plotted as asterisks connected by a dotted curve. (The curve is broken between 4.8 and 8.8 μm since they obtained no data at 7.9 μm .) Crosses connected by the dot-dashed lines represent newly determined *IRAS* HIRES fluxes (this work). The dramatically increasing flux levels with increasing aperture observed at all mid-infrared wavelengths, including bandpasses that exclude PAH feature emission, attest to the presence of both spatially extended PAHs and VSGs in the circumstellar environment of WL 16.

the central source in WL 16. This same method was applied to near-infrared images of WL 16 to derive PSF fit near-infrared photometry as well (Ressler 1992). At all wavelengths, the PSF fit flux contains just photospheric light plus any warm dust within the PSF (<40 AU). Values of these PSF fit fluxes are also tabulated in Table 1.

We present the spectral energy distributions (SEDs) for photometry measured through different-sized apertures for WL 16 in Figure 5. The data have been separated into PSF fit points (*triangles*), 8'' aperture photometry points (*squares and asterisks*), and the 45'' resolution HIRES-processed *IRAS* fluxes (*plus signs*). In the large-aperture (8'') data, the steep drop in flux approaching the wavelength of 9.7 μm from either side was at one time misinterpreted as a very deep silicate absorption feature. The depth of this silicate absorption feature is significantly reduced in the curve connecting just the PSF fit data points, underlining the important contribution of PAH feature emission to the larger aperture photometry.

In the near-infrared, the flux values found within an 8'' aperture (Wilking & Lada 1983) are only slightly higher than the flux values derived through PSF fitting, in contrast to the large observed difference between the PSF and the 8'' aperture photometry values at all mid-infrared wavelengths, through both filters that include and those that exclude PAH features (see Fig. 5). This behavior is as expected of VSG emission: providing only a marginal contribution to near-infrared continuum emission, but being the dominant source of mid-infrared continuum emission. This result also justifies the use of our near-infrared PSF fit fluxes to derive the extinction and intrinsic central source luminosity (see § 4.1).

4. DISCUSSION

4.1. Nature of the Central Source

The spectral type of the central source of WL 16 has recently been determined from high signal-to-noise ratio, moderate-resolution, near-infrared spectroscopy to lie in the range B8–A7, corresponding to a photospheric effective temperature of $8000 \text{ K} \leq T_{\text{eff}} \leq 12,000 \text{ K}$ (Luhman & Rieke 1999). We combine this constraint on the central object's effective temperature with other observational data and theoretical PMS tracks in a self-consistent manner to redetermine both the estimated extinction to the central source and its intrinsic bolometric luminosity, mass, and radius. The low millimeter flux (André & Montmerle 1994; Motte et al. 1998), the lack of near-infrared excess (Moore et al. 1998), and the fact that UV/optical radiation is able to illuminate such a large (900 AU) VSG/PAH-emitting region in the immediate vicinity of WL 16 all lead to the conclusion that the circumstellar material surrounding WL 16 is optically thin at these wavelengths. Furthermore, computations of the continuum SEDs of flared and geometrically thin accretion disks have shown that high accretion rates ($\dot{M} \geq 10^{-6} M_{\odot} \text{ yr}^{-1}$) are required to produce optically thick inner disks around HAeBe stars (Hartmann, Kenyon, & Calvet 1993). For comparison, the upper limit for the inner-disk accretion rate for WL 16 is $\leq 2 \times 10^{-7} M_{\odot} \text{ yr}^{-1}$ (Najita et al. 1996a).

If the circumstellar environment of WL 16 is optically thin in the near-infrared, then the observed extinction along the line of sight toward WL 16 must arise in the intervening ρ Oph cloud, which acts as a foreground screen. We note that this is a radically different physical source picture than one in which it is assumed that all of the energetic UV/visible source photons are intercepted by the immediately surrounding circumstellar material and their energy subsequently reradiated by this same circumstellar material at longer, infrared wavelengths.

In order to determine the value of the intervening extinction, we fix the photospheric temperature of the central source at 9000 K. We include only the near-infrared photometry in the fit, since the near-infrared fluxes are essentially uncontaminated by any classical grain or VSG emission from circumstellar material. We then fit a reddened blackbody (modeling the extinction with the Mathis 1990 curve for molecular clouds) with only two free parameters, A_V and stellar radius, to determine the extinction through the cloud.

The resulting extinction, $A_V = 31$, falls within the range of previously derived values. A strict upper limit can be derived from the line-of-sight, beam-averaged (55'' FWHM) ^{13}CO observations, from which the extinction through the entire cloud in the direction of WL 16 is estimated at $A_V = 70$ mag with a 50% error (B. A. Wilking 1998, private communication). At the other extreme, allowing for a wide range of intrinsic near-infrared source colors, a possible range of $2.0 \leq A_K \leq 2.9$ was found by Carr et al. (1993). A value for $A_V = 31$ toward WL 16 was previously published, derived from its $H-K$ color by Wilking & Lada (1983). The most recent published determination for the extinction toward WL 16 is $A_V = 37$, determined using the near-infrared photometry of Greene & Young (1992) and assuming an intrinsic A star photosphere (Moore et al. 1998).

We argue that our determination of $A_V = 31 \pm 1$ for the extinction toward WL 16 is the most stringent to date.

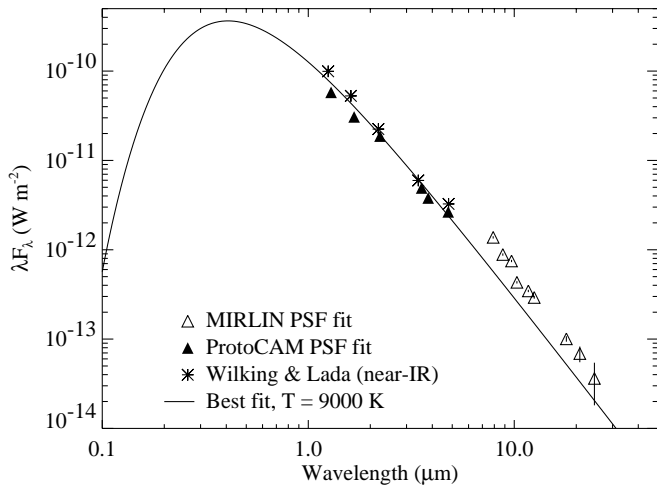


FIG. 6.—Dereddened SED of a $T_{\text{eff}} = 9000$ K, $L_* = 250 L_{\odot}$, $R_* = 6.5 R_{\odot}$ blackbody (photosphere) that represents the central illuminating source of WL 16, seen through an extinction of $A_V = 31 \pm 1$ (see text). Corresponding dereddened PSF fit fluxes are indicated by triangles (filled for near-infrared, open for mid-infrared); dereddened fluxes measured through $8''$ apertures are indicated by asterisks (near-infrared).

Figure 6 shows data and a model that have all been dereddened for an intervening $A_V = 31$ screen using the Mathis (1990) extinction curve. The curve in Figure 6 shows the resulting SED for a $T = 9000$ K blackbody photosphere with a radius of $6.5 R_{\odot}$ at $d = 125$ pc. The triangles represent the dereddened PSF fit data points; the asterisks represent the corrected near-infrared data from Wilking & Lada (1983). Note that the residual silicate absorption feature apparent from the mid-infrared PSF fit photometry in Figure 5 (*solid curve*) completely disappears from the corresponding extinction-corrected PSF fit data plotted in Figure 6. This is especially striking in view of the fact that the mid-infrared fluxes were not included in the fit used to determine the extinction to the source. The dereddened, PSF fit, mid-infrared data points do lie somewhat above the plotted photospheric model curve, however. This slight remaining mid-infrared “excess” may signal the presence of VSGs within less than 40 AU of the central source (within the PSF). Nevertheless, the goodness of the fit suggests that the residual “dip” apparent in the mid-infrared PSF fit data of Figure 5 is caused by the intervening cloud’s silicate absorption, and not by PAH emission.

Strong constraints on the possible values of the derived extinction can be made via the two requirements of (1) matching the shape and magnitude of the dereddened near-infrared flux data to an appropriate blackbody and (2) eliminating the residual $9.7 \mu\text{m}$ silicate absorption feature from the curve joining the PSF fit fluxes in Figure 5. If A_V were greater than ~ 32 , the dereddened data would show a silicate emission feature in the mid-infrared and the near-infrared points would lie on a curve steeper than a blackbody. For $A_V < 30$, fits consistent with a 9000 K blackbody emitter would become problematic. In fact, the derived A_V is relatively insensitive to the assumed temperature: variation from 6000 to 12,000 K produces only a 1 mag change in A_V , since the infrared data are well on the Rayleigh portion of the blackbody curve. Therefore, we can confidently assert that the range of foreground extinction falls within $A_V = 31 \pm 1$.

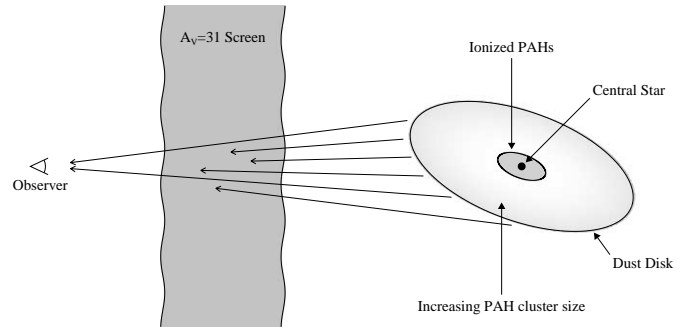


FIG. 7.—Schematic showing the proposed configuration of WL 16. The entire WL 16 system (star plus large disk) is viewed through a portion of the ρ Oph cloud, which acts as an $A_V = 31$ foreground screen. The dust disk around the star is effectively optically thin, so that UV radiation propagates through the entire disk. The inner portions of the disk experience a UV field sufficiently strong to ionize a substantial portion of the PAHs, while a decrease in the field allows a higher fraction of large PAHs to exist at the periphery of the disk.

We can now arrive at a new determination of the bolometric luminosity of WL 16, simply by integrating under the photospheric curve plotted in Figure 6. We find a bolometric luminosity of $250 L_{\odot}$ for an assumed distance of 125 pc. This is much higher than previously published values for the luminosity of WL 16, which range from 10 to $22 L_{\odot}$ for $d = 160$ pc (Young et al. 1986; Wilking et al. 1989). This discrepancy is resolved when one takes into account the very different assumptions that went into the different luminosity determinations. In the absence of evidence to the contrary, previous workers had assumed that all the extinction toward WL 16 was local and circumstellar and that all of the source photons were absorbed and reradiated locally at mid- and far-infrared wavelengths. However, in view of subsequent multiwavelength photometry and spectroscopy, the new source picture that emerges is one in which the extinction is provided by a foreground screen, remote from the source, so that the absorbed photons are reradiated well outside our (or anyone else’s) beam (see Fig. 7 for the schematic cartoon of the source geometry).

Our new bolometric luminosity determination of $250 L_{\odot}$, combined with the spectroscopically determined effective temperature determination of 9000 K, allows placement of WL 16 on the H-R diagram for the first time. Comparison of the position of WL 16 on this diagram with the PMS tracks of Palla & Stahler (1999) yield a source mass of $\sim 4 M_{\odot}$ and a source age of 1.9×10^5 yr. The Siess, Dufour, & Forestini (2000) PMS tracks also give a source mass of $\sim 4 M_{\odot}$, but an age of 1.2×10^6 yr. Previous determinations for the central source’s mass in WL 16 were erroneous for two reasons: (1) PMS tracks for more massive objects ($\geq 2.5 M_{\odot}$) were not yet available and (2) the central objects’s true luminosity was underestimated ($10\text{--}20 L_{\odot}$, rather than $250 L_{\odot}$).

4.2. A Mid-IR-Emitting Disk in WL 16

Previous mid-infrared imaging of WL 16 shows an extended emission region elongated along an approximately northeast-southwest axis (Deutsch et al. 1995; DeVito & Hayward 1998; Moore et al. 1998). This emission has variously been interpreted as originating from a nebula, a torus, a bipolar cavity, or a disk. We consider a “nebula” (meaning an H II region) to be unlikely, given the lack of narrow

spectral features in the near- or mid-infrared and the fact that the central star has a much later spectral type than B3 (Luhman & Rieke 1999). It is also not a reflection nebula, given that scattering is inefficient in the mid-infrared and that the density necessary to show any scattering would require an optically thick disk; we have already argued that WL 16's emission is optically thin. A torus is unlikely, since the intensity profile does not indicate a "hole" in the inner regions of the disk, and a torus would be difficult to maintain physically. A bipolar cavity can be ruled out, since the outflow to create such a cavity was searched for, but not found (Cabrit & André 1991). We propose that the most plausible interpretation of our multiwavelength imaging data set favors the notion that the mid-infrared emission originates from a geometrically thin, equatorial disk.

Under this assumption for the source geometry, the minor-to-major axis ratio is found to be 0.466 ± 0.007 , measured from the images as observed in the four filters that include the PAH emission features. This ratio corresponds to an inclination angle of $62.2^\circ \pm 0.4^\circ$ of the disk to our line of sight, if we assume the disk to be intrinsically circular and to appear elongated only because of projection effects. This value agrees well with the inclination angle ($i = 60^\circ$) deduced for the inner disk ($R \leq 30 R_\odot$) of WL 16 from kinematic modeling of the hot gas ($T = 5000$ K) emitting in the near-infrared CO lines (Dent & Geballe 1991; Carr et al. 1993; Chandler et al. 1993, 1995).

4.3. Properties of the Mid-IR-emitting Disk

It has already been suggested that the mid-IR-emitting dust surrounding WL 16 consists of at least two components, aromatic hydrocarbons and VSGs (Moore et al. 1998). The present observations strongly support this suggestion. The disk of WL 16 is easily visible through all the mid-infrared filters, not just those that contain PAH emission features, although the disk does emit most strongly through those filters that encompass PAHs (Fig. 2). Similar results were found by Moore et al. (1998) upon comparison of their images of WL 16 through filters that contain PAH emission features at 8.2 and 11.3 μm with their 10.2 μm continuum image, which is PAH feature-free. Our results extend this finding to a greater number of wavelengths.

Simple modeling of PAH and VSG emission in the mid-infrared, from spherical distributions of optically thin dust surrounding an 8000 K (12,000 K) central source, suggests that 1% (3.5%) of the starlight would be absorbed by PAHs and 15% (20%) by VSGs. However, these values for the PAHs are highly dependent on the assumed absorption cross sections, and they could be as high as 16.6% (17%) for an 8000 K (12,000 K) central object (Natta & Krügel 1995). For WL 16, we find that $\sim 1\%$ of the 9000 K central source's luminosity, or $2.6 L_\odot$, is emitted by the PAHs and VSGs. At the very least, this low value, relative to the models, rules out spherical distributions of PAHs and VSGs around the source. For comparison, previous authors have estimated $\sim 0.6 L_\odot$ to be contributed by the 7.7–13 μm PAH band emission within a $5''$ beam (Hanner et al. 1992) scaled to $d = 125$ pc, and $1.2 L_\odot$, integrated over the entire disk extent (Moore et al. 1998).

4.3.1. Very Small Grain (VSG) Constituent

Figure 2 shows the extended appearance of WL 16 at 9.7, 10.3, 17.9, 20.8, and 24.5 μm , passbands that exclude PAH

feature emission. Since neither PAHs nor the standard MRN grains can account for this emission, as we argue below, the continuum emitter responsible for this extended mid-infrared emission in the disk of WL 16 must be in the form of the so-called VSGs (Natta & Krügel 1995; DeVito & Hayward 1998; Moore et al. 1998). It has been shown that such VSGs surrounding HAeBe stars are excited by a much broader spectrum of photons than the PAHs and can reprocess stellar radiation into the mid-IR (Natta et al. 1993).

We have already pointed out (see § 4.1) that the systematic mid-infrared excess flux that remains after dereddening the PSF fit photometry requires the presence of VSGs on scales of ≤ 40 AU (see Fig. 6). Similarly, emission from VSGs is required to explain the large spatial extent of WL 16's disk at continuum wavelengths ($R \sim 450$ AU). This is quantitatively illustrated by Figure 8, where intensity cross-cuts of a model disk, consisting of regular ISM grains, are compared with the actual, observed intensity profiles of WL 16's disk. The model disk intensity profiles, kindly provided by Dr. Barbara Whitney, use a three-dimensional Monte Carlo code described in Wood et al. (2002) and include both scattering and emission by standard interstellar grains (Kim, Martin, & Henry 1994) at mid-infrared wavelengths. The model shown is for a $0.01 M_\odot$ flared disk (the maximum disk mass allowed by millimeter observations), inclined at 60° to our line of sight, at a distance of 125 pc, illuminated by a central source of $250 L_\odot$ and $T_{\text{eff}} = 9000$ K. The disk density structure is as described in Wood et al. (2002), except that the inner radius is set by the dust destruction radius for a $T_{\text{eff}} = 9000$ K central source and the disk's outer radius is determined by the observations presented here. Note that emission from standard, interstellar grains at large radii from the central source would be undetectable according to the models, in stark contrast to the observed emission. Standard, interstellar grains cannot, therefore, be responsible for the appearance of WL 16's disk at large radii through the filters that exclude PAH emission.

Additional qualitative proof of this assertion is provided in Figure 3. A comparison of the 9.7, 10.3, 17.9, 20.8, and 24.5 μm flux profiles (none of which should have significant PAH emission) with the fiducial 11.7 μm profile suggests a rather constant ratio as a function of distance from the center, despite any differences in the absolute surface brightness values. This also holds true in the fully two-dimensional case, where ratios of any pair of images, including the 10.3/20.8 μm ratio image (not shown), are generally very flat outside of the ionized PAH core. This behavior is consistent with the emission expected from VSGs, but it is inconsistent with the emission properties expected from classical grains. It also suggests that the PAHs and VSGs are well mixed.

4.3.2. PAH Ionization, Hydrogenation, and Size Effects in the WL 16 Disk

The color ratio images presented in Figure 4 can give some qualitative indication as to the charge state, amount of hydrogenation, and size of the emitting PAH molecules. Quantum mechanical modeling and laboratory studies of PAH emission have shown that the charge state of the PAH has an important effect on the emitted IR spectrum. In particular, the intensities of the C—C stretching and C—H in-plane bending modes, which fall in the 6–9 μm range, are

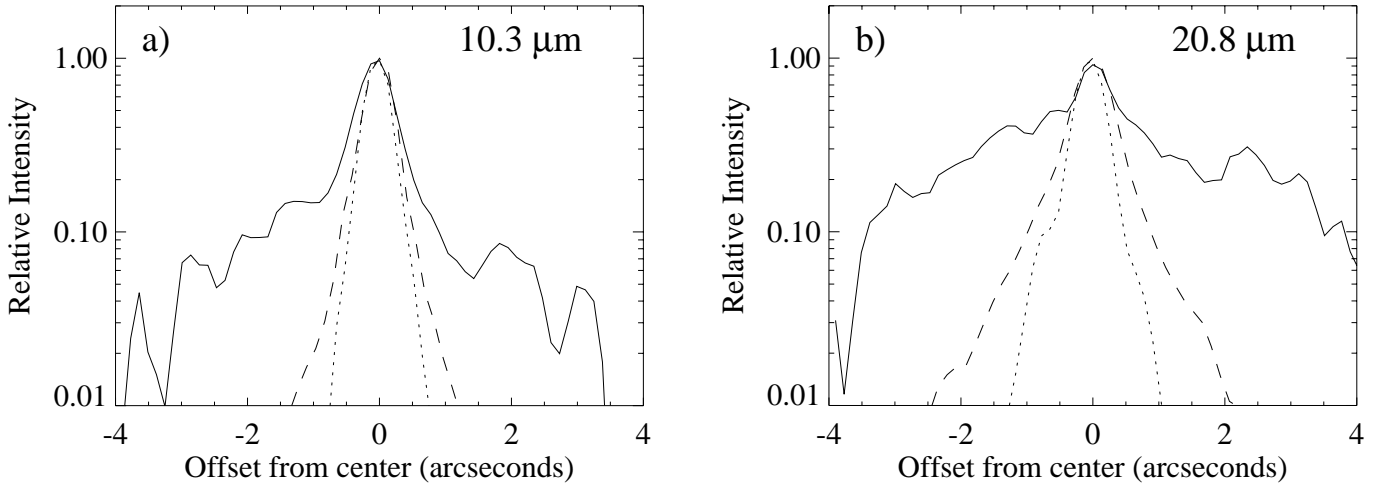


Fig. 8.—Plots of the observed continuum intensity profile of the disk of WL 16 along its major axis, compared with models of a disk composed only of classical interstellar grains: data and model for (a) 10.3 and (b) 20.8 μm . *Solid curves*, Observed profiles; *dashed curves*, interstellar grain-only disk model; *dotted curves*, observed PSFs. While the disk models are clearly more extended than the observed PSFs, they underpredict the observed flux from WL 16's disk by an order of magnitude or more at radii greater than an arcsecond, and their steep slope is incompatible with the broad observed profiles. The presence of VSGs is required to account for the large spatial extent of non-PAH emission.

generally an order of magnitude stronger in PAH cations (singly ionized PAHs) than in neutral PAHs (Joblin et al. 1996; Langhoff 1996; Hudgins & Allamandola 1995a, 1995b). Viewed in this context, it is therefore not surprising that the 7.9/8.8 μm flux ratio shown in the top panels of Figure 4 is essentially constant over the entire emitting region of the WL 16 disk, since both of these features (at 7.7 and 8.6 μm) originate from positively charged PAHs.

DeVito & Hayward (1998) found a central peaking of the continuum-subtracted 8.6/11.3 μm feature ratios in the disk of WL 16. We confirm this in the middle left panel of Figure 4, which shows the 8.8/11.7 μm flux ratio image. In contrast to the featurelessness of the 7.9/8.8 μm ratio image, a distinct enhancement within the central $\pm 1''.5$ core is observed (see also Fig. 3).

Recent quantum mechanical calculations show that the 8.6 μm feature originates mostly from C—H in-plane bending modes of positively charged PAHs, whereas the 11.3 μm feature originates from C—H out-of-plane bending modes of predominantly neutral and anionic PAHs (Bakes et al. 2001). The observed contrast in the 8.8/11.7 μm flux ratio image and crosscut of Figure 4 may be interpreted as a change in charge state of the PAHs from positively ionized in the central regions to neutral in the outer regions (Joblin et al. 1996; DeVito & Hayward 1998).

The physical conditions required for the 11.3 μm feature to originate mainly from neutral, and not positively charged, PAHs are expressed by the constraint, $G_0/n_e \leq 10^3$, where G_0 is the UV radiation field (6–13.6 eV) in units of 1.6×10^{-3} ergs cm^{-2} s^{-1} and n_e is the electron density in units of cm^{-3} (Bakes et al. 2001). Of course, the central Herbig Ae star is the photoionizing and UV source for the WL 16 disk. The calculated UV radiation field in the WL 16 disk at different distances from the central source is $G_0 = 1.2 \times 10^5$ at $0''$ – $1''$, 2×10^4 at $1''$ – $2''$, 4.8×10^3 at $2''$ – $4''$, and 1.6×10^3 at $4''$ – $6''$ (DeVito & Hayward 1998). Combining these values of the UV flux with the 11.3 μm feature neutrality constraint leads to derived electron densities in the WL 16 disk decreasing from $n_e \sim 100 \text{ cm}^{-3}$ in the central regions to $n_e \sim 10 \text{ cm}^{-3}$ in the outer regions.

The bottom panels of Figure 4 show the 12.5/11.7 μm flux ratios. The most interesting feature in this image is the gradual enhancement of the 12.5/11.7 μm ratio toward the disk edges. Two possible explanations for this enhancement are increasing molecular size and increasing hydrogenation toward the disk edges.

It has been shown that partially hydrogenated, small (<25 C atoms) PAHs, as well as large PAHs with one, two, or three adjacent H atoms, can contribute to the 11.3 μm feature (Cohen, Tielens, & Allamandola 1985; Mortera & Low 1983). However, only relatively large PAHs with one, two, or three adjacent H atoms are needed to produce the 12.7 μm feature (Duley & Williams 1981). Quantum mechanical calculations show that the 12.7 μm PAH feature strength increases with molecule size (Bakes et al. 2001). Therefore, one possible interpretation for the enhancement of the 12.5/11.7 μm flux ratio at the disk's edges is the growth of larger PAHs (≥ 50 – 80 C atoms) at greater distances from the central ionizing source.

Alternatively, since the 11.3 μm feature originates from PAHs with isolated H atoms (Cohen et al. 1985), whereas the 12.7 μm feature requires two adjacent hydrogen atoms on the aromatic ring (Verstraete et al. 1996), the slight increase in the 12.5/11.7 μm ratio apparent toward the edges of the WL 16 disk might be due to increasing hydrogenation. Increasing hydrogenation may take place because of lower collision rates with electrons that would knock away H atoms, as a result of lower n_e at the disk edges and/or lower UV flux to dissociate H atoms from PAHs.

4.3.3. Disk Asymmetry

The intensity profiles along the disk's major axis presented in Figure 3 show the presence of an asymmetry in emission strength with respect to mirror reflection about the central position at all observed wavelengths. This asymmetry occurs at angular separations between $1''$ and $2''.5$ from the central position, corresponding to radii of $125 \text{ AU} \leq r \leq 300 \text{ AU}$. Since this asymmetry is observed at all wavelengths, it is likely due to either a column density

enhancement in one side of the disk or a gap in the other. We do not have enough information to distinguish between these two possibilities.

Although it is tempting to invoke the presence of embedded planets to account for the observed disk asymmetry due to gravitational perturbations, the large radii ($125 \text{ AU} \leq r \leq 300 \text{ AU}$) at which this asymmetry is observed conflicts with all current theories, which predict $\sim 20 \text{ AU}$ as a typical outer boundary for planet formation from an accretion disk. Furthermore, any planetary time formation timescale at such large radii would exceed the inferred age of the central star. Nevertheless, objects a few meters to hundreds of meters in size could have had time to form at these radii (Kenyon & Luu 1999).

4.3.4. Disk Lifetime

One intriguing problem is the question of how the PAH/VSG disk we observe is replenished, since even at the disk's extremities, the timescales for blowing small particles out of the system by radiation pressure are only years. Condensation from the gas phase is highly unlikely, given the low gas densities throughout most of the disk and the high activation energies required for PAH synthesis, which lead most researchers in the field to conjecture that PAHs are formed on the surface of grains. This leads us to the suggestion that the most likely scenario for replenishment of the PAHs/VSGs in the disk of WL 16 is from the breakup of larger bodies, such as comets or Kuiper belt objects, or from UV or shock processing of larger grains, as has recently been suggested by Duley (2000). The presence of PAHs in a possible planet-forming system has interesting implications for the potential seeding of planetary systems with organic materials, and it is also consonant with the discovery of PAHs in meteorites.

5. CONCLUSIONS

We have presented diffraction-limited images and photometry of the disk surrounding the Herbig Ae star WL 16 at nine mid-infrared wavelengths, as well as photometry of the central star at five additional near-infrared wavelengths. From our newly derived SED for this source, we find that the central star and its disk are observed through a foreground screen, which provides an extinction of $A_V = 31 \pm 1 \text{ mag}$. We find that the star itself has a bolometric luminosity of $250 L_\odot$ (at an assumed 125 pc distance)

and that the disk contributes $\approx 1\%$ as a result of VSG and PAH feature emission.

The unprecedented spatial resolution of the mid-infrared images presented here allows us to confirm the presence of ionized PAHs in the central disk regions, and we report the discovery of a population of larger ($\geq 50\text{--}80 \text{ C atoms}$) and/or more hydrogenated PAHs at the disk's periphery. We confirm that a population of graphitic VSGs is required to account for the observed large disk extent through the five mid-infrared filters, which exclude the wavelengths of the PAH emission features. These VSGs are also required to explain the observed mid-infrared excess emission within the unresolved inner core ($\leq 0.3''$) of the WL 16 images.

The disk size is found to be $7'' \times 3.5''$, corresponding to a deprojected disk diameter of 900 AU at the source. The disk inclination is found to be $62^\circ \pm 2^\circ$ to our line of sight at P.A. 60° . We find an asymmetry in the disk, at all observed mid-IR wavelengths, at $1''\text{--}2.5''$ from the central source. Finally, continuous replenishment of disk material, possibly from collisions of larger parent bodies, is required to maintain the PAH/VSG disk, which would otherwise be destroyed by blowout by radiation pressure on timescales of years.

We wish to thank Emma Bakes, Timothy Brooke, Lynne K. Deutsch, Tom Greene, Martha Hanner, Antonella Natta, Deborah Padgett, Sue Terebey, Michael Werner, and Bruce Wilking for helpful discussions during the preparation of this paper. Barbara Whitney kindly provided realistic disk models consisting of interstellar grains for direct comparison with the observations presented in this paper. M. E. R. thanks Fred Chaffee and the entire Keck Observatory staff for their enthusiasm, patience, and assistance in making it possible to use MIRLIN on the Keck II Telescope. Portions of this work were carried out at the Jet Propulsion Laboratory, California Institute of Technology, under contract with the National Aeronautics and Space Administration. Development of MIRLIN was supported by the JPL Director's Discretionary Fund, and its continued operation is funded by an SR+T award from NASA's Office of Space Science. M. B. gratefully acknowledges financial support from grants NSF AST 97-53229, NSF 0096087 (Career), and NSF AST 02-06146, and from NASA's Long-Term Space Astrophysics Research Program, NAG 5-8412, which made her contributions to this work possible.

REFERENCES

- Adams, F. C., Lada, C. J., & Shu, F. H. 1987, *ApJ*, 312, 788
 André, P., & Montmerle, T. 1994, *ApJ*, 420, 837
 Bakes, E. L. O., Tielens, A. G. G. M., Bauschlicher, C. W., Jr., Hudgins, D. M., & Allamandola, L. J. 2001, *ApJ*, 560, 261
 Barsony, M., Kenyon, S. J., Lada, E. A., & Teuben, P. J. 1997, *ApJS*, 112, 109
 Brooke, T. Y., Tokunaga, A. T., & Strom, S. E. 1993, *AJ*, 106, 656
 Cabrit, S., & André, P. 1991, *ApJ*, 379, L25
 Carr, J. S., Tokunaga, A. T., Najita, J., Shu, F. H., & Glassgold, A. E. 1993, *ApJ*, 411, L37
 Chandler, C. J., Carlstrom, J. E., & Scoville, N. Z. 1995, *ApJ*, 446, 793
 Chandler, C. J., Carlstrom, J. E., Scoville, N. Z., Dent, W. R. F., & Geballe, T. R. 1993, *ApJ*, 412, L71
 Cohen, M., Tielens, A. G. G. M., & Allamandola, L. J. 1985, *ApJ*, 299, L93
 de Geus, E. 1992, *A&A*, 262, 258
 de Geus, E., de Zeeuw, P., & Lub, J. 1989, *A&A*, 216, 44
 Dent, W. R. F., & Geballe, T. R. 1991, *A&A*, 252, 775
 Deutsch, L. K., Hora, J. L., Butner, H. M., Hoffman, W. F., & Fazio, G. G. 1995, *Ap&SS*, 224, 89
 DeVito, B., & Hayward, T. L. 1998, *ApJ*, 504, L43
 Draine, B. T., & Anderson, N. 1985, *ApJ*, 292, 494
 Duley, W. W. 2000, *ApJ*, 528, 841
 Duley, W. W., & Williams, D. A. 1981, *MNRAS*, 196, 269
 Emerson, J. P., Moore, T. J. T., Skinner, C. J., & Meixner, M. M. 1996, in *The Role of Dust in the Formation of Stars*, ed. H. U. Käuffl & R. Siebenmorgen (Heidelberg: Springer), 23
 Greene, T. P., & Young, E. T. 1992, *ApJ*, 395, 516
 Hanner, M. S., Brooke, T. Y., & Tokunaga, A. T. 1995, *ApJ*, 438, 250
 Hanner, M. S., Tokunaga, A. T., & Geballe, T. R. 1992, *ApJ*, 395, L111
 Hartmann, L., Hewett, R., & Calvet, N. 1994, *ApJ*, 426, 669
 Hartmann, L., Kenyon, S. J., & Calvet, N. 1993, *ApJ*, 407, 219
 Herbig, G. H. 1994, in *ASP Conf. Ser. 62, The Nature and Evolutionary Status of Herbig Ae/Be Stars*, ed. P. S. Thé, M. R. Perez, & P. J. van den Heuvel (San Francisco: ASP), 3
 Hudgins, D. M., & Allamandola, L. J. 1995a, *J. Phys. Chem.*, 99, 3033
 ———. 1995b, *J. Phys. Chem.*, 99, 8978
 Joblin, C., Tielens, A. G. G. M., Geballe, T. R., & Wooden, D. H. 1996, *ApJ*, 460, L119
 Kenyon, S. J., & Luu, J. X. 1999, *ApJ*, 526, 465
 Kim, S.-H., Martin, P. G., & Hendry, P. D. 1994, *ApJ*, 422, 164
 Knude, J., & Høg, E. 1998, *A&A*, 338, 897

- Lada, C. J. 1987, in IAU Symp. 115, Star Forming Regions, ed. M. Peimbert & J. Jugaku (Dordrecht: Reidel), 1
- Lada, C. J., & Wilking, B. A. 1984, *ApJ*, 287, 610
- Langhoff, S. R. 1996, *J. Phys. Chem.*, 100, 2819
- Luhman, K. L., & Rieke, G. H. 1999, *ApJ*, 525, 440
- Lynch, D. K., & Mazuk, S. 2000, in ASP Conf. Ser. 196, Thermal Emission Spectroscopy and Analysis of Dust, Disks, and Regoliths, ed. M. L. Sitko, A. L. Sprague, & D. K. Lynch (San Francisco: ASP), 127
- Mathis, J. S. 1990, *ARA&A*, 28, 37
- Mathis, J. S., Rumpl, W., & Nordsieck, K. H. 1977, *ApJ*, 217, 425
- Mortera, C., & Low, M. J. D. 1983, *Carbon*, 21, 283
- Moore, T. J. T., Emerson, J. P., Skinner, C. J., & Meixner, M. M., Arens, J. F., & Jernigan, J. G. 1998, *MNRAS*, 299, 1209
- Motte, F., André, P., & Neri, R. 1998, *A&A*, 336, 150
- Najita, J., Carr, J. S., Glassgold, A. E., Shu, F. H., & Tokunaga, A. T. 1996a, *ApJ*, 462, 919
- Najita, J., Carr, J. S., & Tokunaga, A. T. 1996b, *ApJ*, 456, 292
- Natta, A., & Krügel, E. 1995, *A&A*, 302, 849
- Natta, A., Prusti, T., & Krügel, E. 1993, *A&A*, 275, 527
- Palla, F., & Stahler, S. W. 1999, *ApJ*, 525, 772
- Ressler, M. E. 1992, Ph.D. thesis, U. Hawaii
- Ressler, M. E., Werner, M. W., Van Cleve, J., & Chou, H. A. 1994, *Exp. Astron.*, 3, 277
- Siebenmorgen, R., & Krügel, E. 1992, *A&A*, 259, 614
- Siess, L., Dufour, E., & Forestini, M. 2000, *A&A*, 358, 593
- Tanaka, M., Sato, S., Nagata, T., & Yamamoto, T. 1990, *ApJ*, 352, 724
- Tokunaga, A. T., Sellgren, K., Smith, R. G., Nagata, T., Sakata, A., & Nakada, Y. 1991, *ApJ*, 380, 452
- Verstraete, L., Puget, J. L., Falgarone, E., Drapatz, S., Wright, C. M., & Timmermann, R. 1996, *A&A*, 315, L337
- Waters, L. B. F. M., & Waelkens, C. 1998, *ARA&A*, 36, 233
- Wilking, B. A., & Lada, C. J. 1983, *ApJ*, 274, 698
- Wilking, B. A., Lada, C. J., & Young, E. T. 1989, *ApJ*, 340, 823
- Wood, K., Wolff, M. J., Bjorkman, J. E., & Whitney, B. 2002, *ApJ*, 564, 887
- Young, E. T., Lada, C. J., & Wilking, B. A. 1986, *ApJ*, 304, L45